Applied Physics A (2020) 126:910
https://doi.org/10.1007/s00339-020-04093-1

Applied Physics A
Materials Science & Processing

Switching of linear and nonlinear optical parameters in $As_{35}Se_{65}$ thin films upon annealing at both above and below T_g

P. Priyadarshini[1] · D. Sahoo[1] · A. Aparimita[2] · D. Alagarasan[3] · R. Ganesan[3] · S. Varadharajaperumal[4] · Ramakanta Naik[1]

Received: 3 September 2020 / Accepted: 19 October 2020 / Published online: 2 November 2020

Abstract

The present manuscript investigated the effect of thermal annealing at 150 °C (below T_g) and 250 °C (above T_g) on the nonlinear as well as linear optical parameters and structural changes of the thermally evaporated $As_{35}Se_{65}$ thin films. The structural investigation was done by X-ray diffraction, Raman spectroscopy, X-ray photoelectron spectroscopy, whereas the surface morphology was studied by field emission scanning electron microscopy. The optical transmission and reflection spectra over the wavelength range 500–1200 nm were used to calculate the optical parameters. The optical energy gap, Urbach energy, optical density, skin depth, Tauc parameters for the as-deposited and annealed $As_{35}Se_{65}$ films were estimated and discussed in terms of density of defect states and disorders. The indirect optical energy gap decreased for 150 °C annealed film and abruptly increased for 250 °C annealed film as compared with the as-prepared film. The Swanepoel envelope method, WDD model, and Sellemeire postulates were employed for analysis of refractive index, static refractive index, dispersion energy, oscillator wavelength, oscillator energy, and dielectric constant. The non-linear refractive index and third-order susceptibility were also estimated with the help of empirical relations which showed opposite changes for the two annealing temperatures. The tunable optical properties can be applied for several optoelectronic application.

Keywords Thin films · Annealing · Optical parameter · Refractive index · Non-linear optical properties · Bandgap

1 Introduction

In the recent era of science and technology, the amorphous chalcogenide materials have a wide range of applications in optoelectronics, phase change memory device, solar cells, sensor technology, telecommunication sector, and many more [1–3]. These chalcogenide thin films have large nonlinear optical behavior than their oxide counterpart due to the presence of heavy chalcogen atoms which have vibrational bonding at low energy. This unique behavior brings large transparency in the mid-IR region that is useful for optical fibre [4]. Among the chalcogenide alloys, Se containing As-based chalcogenides has large third-order optical nonlinear behavior because of the available double lone pair electrons [5]. Such properties can be modified by changing the composition of the films [6], treating the films by energetic ions [7], annealing at different temperatures [8], photo-irradiation [9], gamma irradiation [10], and many more techniques.

Among the above methods, thermal annealing process is well-known for the study on the depletion of inherent defects present in the vitreous state as well as the phase transformation effects. Such method allows to diffuse the composite system and facilitates the change in the physical and chemical properties of the systems. Heat treatment is a simple method to measure the reduction in the inherent defects in the amorphous state and amorphous-crystalline phase transformation [11]. The relaxation of the film into equilibrium condition is accelerated by thermal annealing than the conventional room temperature. It is to be noted that the relaxation time at normal room temperature for non-annealed films is very high [12]. The relaxation time

✉ Ramakanta Naik
ramakanta.naik@gmail.com

[1] Department of Engineering and Material Physics, ICT-IOC, Bhubaneswar 751013, India

[2] Department of Physics, Utkal University, Bhubaneswar 751004, India

[3] Department of Physics, Indian Institute of Science, Bangalore 560012, India

[4] Centre for Nano Science and Engineering, Indian Institute of Science, Bangalore 560012, India

is less at a characteristic temperature called as glass transition temperature (T_g) which is an important parameter for characterization of glassy state. In a glassy material, the lowest temperature at which the defects anneal away from the system is the glass transition temperature (T_g). Thus, the density of defects depends upon the glass transition temperature. T_g is related to the rigidity of the glassy network which is associated with the physical parameters like mean coordination number, cohesive energy, fixed value of viscosity ($\mu(T_g) \approx 10^{13}$ poise) for chalcogenides, dissociation energy etc. [13]. Hence, for chalcogenide glassy materials, the annealing temperature was selected by considering T_g of the material. The annealing of $As_{50}Se_{50}$ at a temperature 150 °C (T_g for $As_{50}Se_{50}$ is 156 °C [14]) caused atomic rearrangements that facilitated the formation of more homogeneous surface compositions and enhanced the concentration of heteropolar bonds over homopolar ones [15]. Tsvetkova et al. have studied that annealing at a temperature near T_g, affected the optical reflectivity and created a rippled surface, which depends on the concentration of As [16]. Similarly, the increase in annealing temperature and duration leads to the transformation of structural properties by the formation of $AsSe_3$ pyramidal units with low surface roughness [17]. In the PLD based $As_{50}Se_{50}$ system, the thermal annealing reduced the structural and electronic defects [18]. Annealing near T_g brings the structural polymerization through the conversion of the homopolar bond to the heteropolar bond. The non-linear optical and dispersion parameter in As–Se–Sb films got largely affected by the thermal annealing process [19]. Due to annealing near its T_g, enhances the linear optical properties of As_2Se_3 [20]. Annealing improves the performance of Ge–Se thin film which is used for device applications [21]. The femtosecond laser irradiation on $As_{35}Se_{65}$ thin films resulted in the submicron gratings used for optical devices [22]. Due to the lack of systematic study on the tailoring of the linear and nonlinear optical parameters of $As_{35}Se_{65}$ film by annealing below and above glass transition temperature encouraged us for the present study.

The present study is focused on the analysis of both nonlinear and linear optical parameters of $As_{35}Se_{65}$ thin film annealed at 150 °C (below T_g) and 250 °C (above T_g). The various experimental characterizations were done to study the structural, optical, morphological behaviors. The single oscillator Wemple Di-Domenico model was used to obtain the two energies such as oscillator and dispersion energy. The obtained linear parameters were used to deduce the nonlinear constants by applying the semi-empirical Miller's formula. The various linear optical constants (oscillator energy, optical band gap, dispersion energy, extinction coefficient, refractive index, absorption coefficient, optical density) and nonlinear optical parameters (third-order nonlinear susceptibility, nonlinear refractive index) have shown opposite nature for the two-annealing temperatures.

2 Experimental procedures

2.1 Details of thin film preparation

Bulk $As_{35}Se_{65}$ alloy was prepared by melt quenching method through the mixing of As and Se by taking stoichiometric amount in a quartz ampoule. After that, the ampoule was sealed under high vacuum condition and was put inside a furnace. The ampoules were heated in the furnace till 900 °C, at a slower rate of about 3–4 °C/min, and held at that temperature for 20 h. At the time of heating, the ampules were constantly shaken to achieve homogeneity. Then the ampule was brought out from the furnace and was rapidly quenched with ice-cold water. After that, the ampule was broken and the bulk alloy was removed for the thin film preparation. In the thermal evaporation procedure, the thin films were prepared from the bulk using the vacuum coating unit (HIND–HIVAC Model 12A4D). The thickness of the film (~ 800 nm) and rate of deposition (0.5 nm/s) were regulated through the crystal thickness monitor. The deposition process took place on clean glass substrates under 10^{-5} Torr vacuum. The as-prepared thin film was subjected to thermal annealing at 150 °C (below T_g) and 250 °C (above T_g) for 2 h.

3 Experimental techniques

To get the structural information, the X-ray diffraction (XRD) was done by Bruker D8 Advance, Cu-Kα radiation ($\lambda = 1.54$ Å) for the three films. The Raman spectroscopy measurements were performed in the LabRAM HR system by 514.5 nm argon laser with a CCD detector in backscattering mode in a range of 50–400 cm^{-1} to get more structural details. The constituent elements in the film such as As and Se was checked by energy-dispersive X-ray analysis (EDAX) and the surface morphology of the films were studied by Field emission scanning electron microscope (FESEM). The scanning of the films was done at 1 cm^2 size exposure area by 20 kV voltage and 40 mA emission current at a pressure of 2×10^{-7} Torr. The data was recorded 3–4 times at various positions to minimize the errors. The optical properties were studied from the reflectance and transmittance data obtained by UV–Vis spectrometer (IFS66v/S) in 500–1200 nm wavelength range at room temperature. The chemical bonding modifications induced by annealing at each temperature were recorded in XPS (Axis Ultra, Kratos Analytical, UK) measurement. The core-level XPS spectra were taken by Al K_α X-rays (1486.6 eV) with a vacuum of 2×10^{-9} Torr. As the prepared films are of insulating glassy nature, the required

charge correction was done with C1s binding energy (BE) of 284.6 eV [23, 24]. The original BE data correction was done using the calibration factor. The scan was performed at different portions of the films to reproduce the data.

4 Results and discussion

4.1 Structural analysis

The XRD patterns of the three films (as-prepared and 150 °C, 250 °C annealed) are presented in Fig. 1 which shows the absence of any sharp crystalline peaks. This confirms the amorphous structure of the studied films from which we can conclude that the annealing the film at both below and above T_g does not bring any change in its amorphous form. The humps appeared at different θ values are due to the glass substrates used for the film preparation [25, 26].

The Raman spectra for the as-prepared and 150 °C, 250 °C annealed films show peaks at different wavenumbers, as shown in Fig. 2. The peak located at 220 cm^{-1} is due to the As–Se vibration of the pyramidal structure $AsSe_{3/2}$ symmetric stretching units [27]. However, there is a shoulder peak at 234 cm^{-1} which is assigned to the vibrations of As–Se structural units [28]. The peak intensity of these two peaks increased for the 150 °C annealed film, while it decreased for the 250 °C annealed film. In addition, the position of 234 cm^{-1} peak shifted to 243 cm^{-1} for the 250 °C annealed film. Therefore, we have observed the opposite change in intensity for the two films annealed at below T_g and above T_g which clearly indicates the different amorphization in the two films. There is another low-intensity peak at 462 cm^{-1} which may be for Se–Se vibrational bonds which disappears at 250 °C annealing. The Se–Se homopolar bond

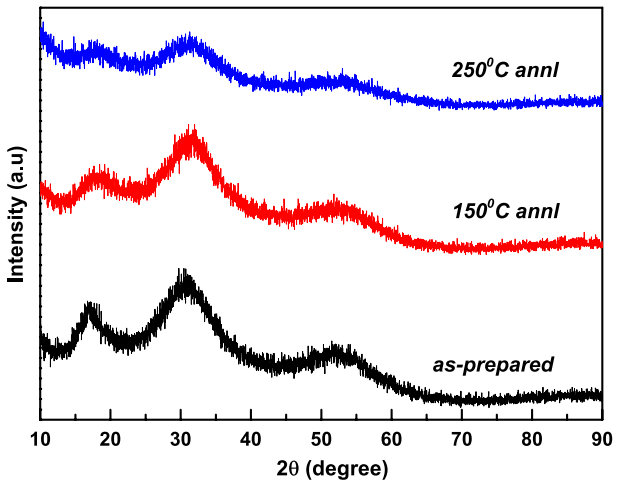

Fig. 1 XRD patterns of studied thin films

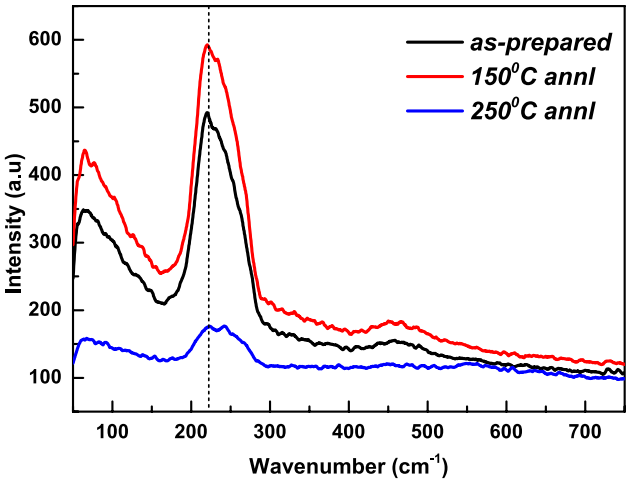

Fig. 2 Raman spectra of the studied thin films

acts as a defect state in the system. As temperature increases, the defect present inside the system annealed away which reduced the disorder. The intensity for 150 °C annealed film is more than that of 250 °C annealed one infers the less disorder in 250 °C annealing than 150 °C annealing.

5 Morphology study

The constituent As and Se elements of both as-prepared, 150 °C and 250 °C annealed films were verified by EDAX picture as presented in Fig. 3. The respective peak corresponds to different elements and the corresponding film composition is approximately same and within 4% error as compared to the calculated value (Table 1).

The FESEM pictures at 200 nm scale of the as-prepared and 150 °C, 250 °C annealed $As_{35}Se_{65}$ films are shown in Fig. 4. The picture shows the homogeneous and smooth nature of the as-prepared film. The annealing effect on surface morphology is visible from these pictures as we can see that the annealed film possesses some agglomerations. We have observed the dense granules in the 150 °C annealed film and less granules in the 250 °C annealed film. The agglomeration increased upon annealing. Therefore, the annealed films are rough in nature.

5.1 Optical study

5.1.1 Linear optical property analysis

5.1.1.1 Transmittance (*T*) and reflectance (*R*) The optical transmittance is the property of the material that relates the capability of transmitting the electromagnetic waves through the system. This property is contributed to several applications in the field of optical and electronic devices.

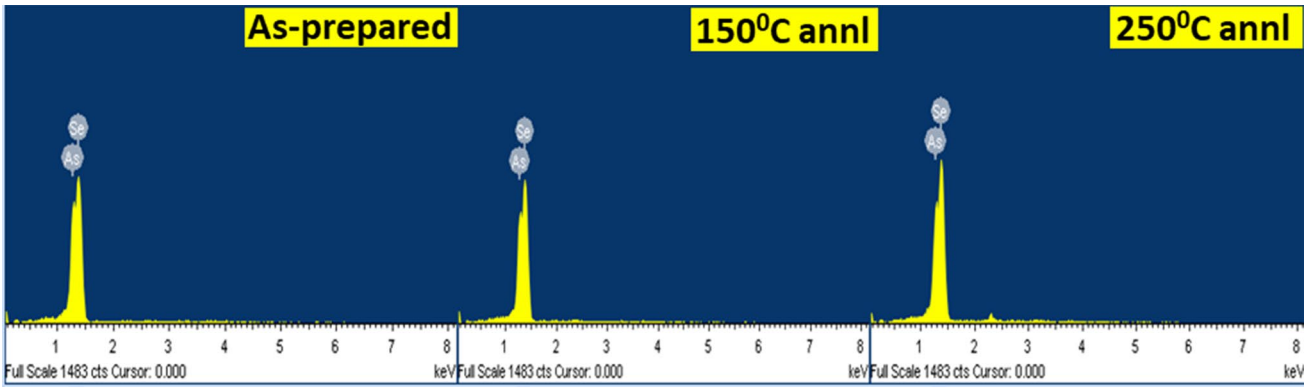

Fig. 3 EDAX picture of as-prepared, 150 °C and 250 °C annealed thin films

Table 1 Composition of as-prepared and annealed $As_{35}Se_{65}$ films

Sample	Asp-$As_{35}Se_{65}$		150 °C annealed		250 °C annealed	
Element	Wt.%	At.%	Wt.%	At.%	Wt.%	At.%
As L	40.07	38.49	40.48	38.92	40.63	39.01
Se L	59.93	61.51	59.52	61.08	58.37	60.99
Total	100.00	100.00	100.00	100.00	100.00	100.00

The reflectance and transmittance spectra of as-prepared, 150 °C and 250 °C annealed films from the UV–Vis spectroscopic measurement are shown in Fig. 5.

From Fig. 5, the equispaced oscillatory fringes in the transmission spectra over the longer wavelength region (700–1150 nm) give a quite clear indication regarding uniformity in the thickness throughout the film [29]. It was observed that the transmittance of the films increased with wavelength. Furthermore, annealing below glass transition temperature (T_g), i.e., 150 °C causes a slight decrease in transmittance from 61% (as-prepared) to 60%, whereas an increase in transmittance to 63% has been seen for annealing above the T_g, i.e., 250 °C.

Figure 5 also depicts the shifting of absorption edge towards the longer wavelength side (redshift) for the 150 °C annealed film, whereas it shifts towards lower wavelength region (blue shift) for 250 °C annealed film as compared to the as-deposited film. The reflectance spectra showed the opposite behavior as compared to the transmittance curve.

5.1.1.2 Absorption coefficient (*α*) The absorption coefficient (α) provides information regarding the optical energy bandgap and band tailing parameters of the amorphous system. The α value of the thin films over strong absorption region was evaluated using both the T and R spectra by [30]:

$$\alpha = \frac{1}{d} \ln \frac{(1-R)^2}{T}, \tag{1}$$

where d represents the film thickness (~ 800 nm). The behavior of α for $As_{35}Se_{65}$ thin film at the two-annealing temperature with wavelength is shown in Fig. 6. It is found that the α value is of 10^4 cm^{-1} order and decreases with wavelength which indicates the better transparency of the films and radiation can travel at a much faster and easier way through it. The variation of α for the 150 °C and 250 °C annealed films are opposite in nature, i.e., 150 °C annealed film shows redshift, whereas 250 °C annealed film shows blue shift.

5.1.1.3 Extinction coefficient (*k*) The parameter extinction coefficient measures the loss of light that got absorbed or scattered per unit volume. Using the value of absorption coefficient (α), the extinction coefficient of the system can be estimated through the relation given as [31]

$$k = \frac{\alpha\lambda}{4\pi}. \tag{2}$$

Figure 6 (inset plot) represents the behavior of k with the energy of incident radiation ($h\nu$). From the plot, it can be inferred that the high value of k at high energy region signifies the opaque-ness at this range. After the absorption edges, it can be seen that k has a very small value, which indicates better transmittance. Here also we have observed the increase and decrease in k value with annealing at 150 °C and 250 °C, respectively. The change in the value of the extinction coefficient leads to modify the nonlinear parameters of the materials [32].

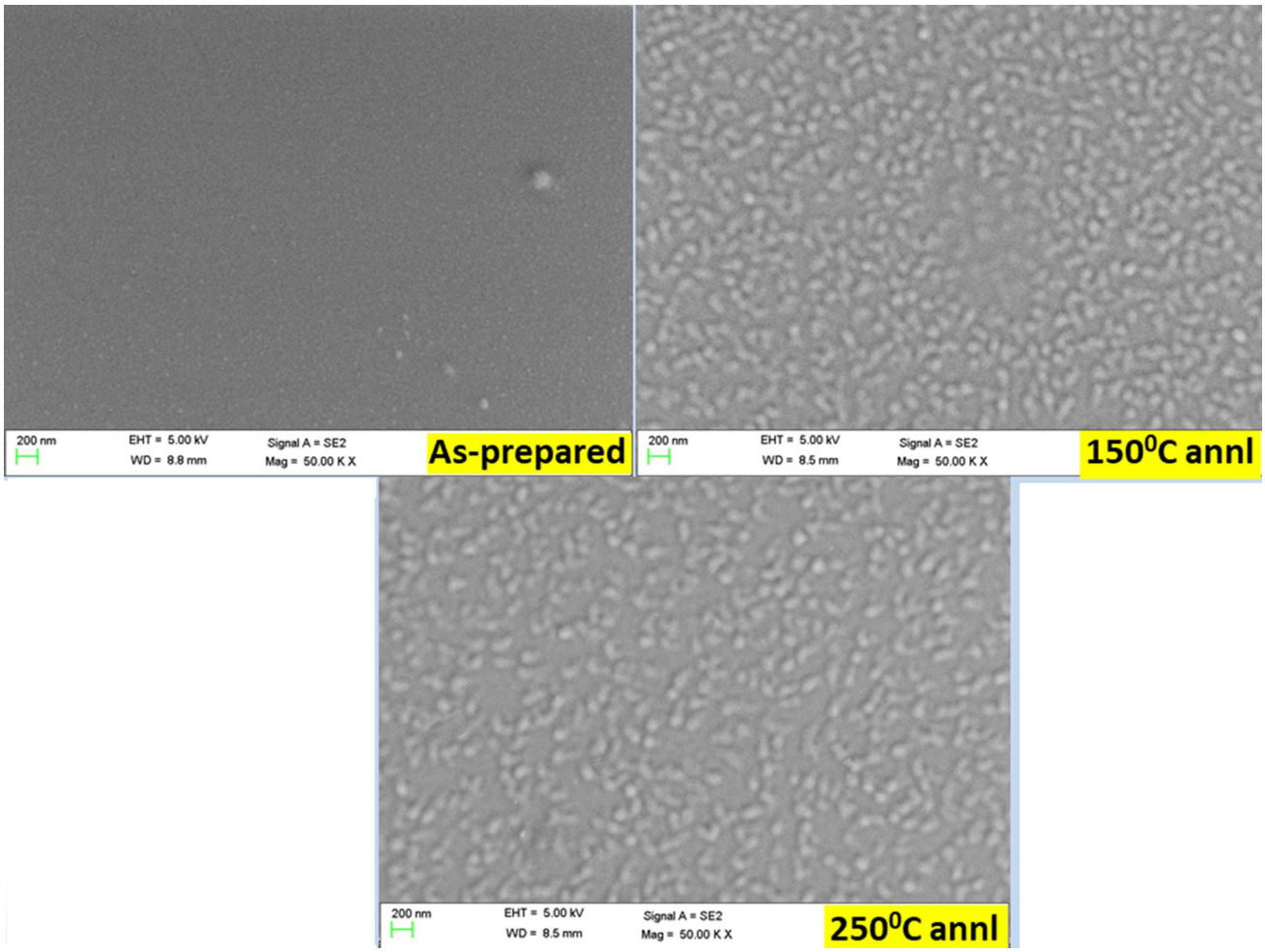

Fig. 4 FESEM picture of as-prepared and annealed thin films

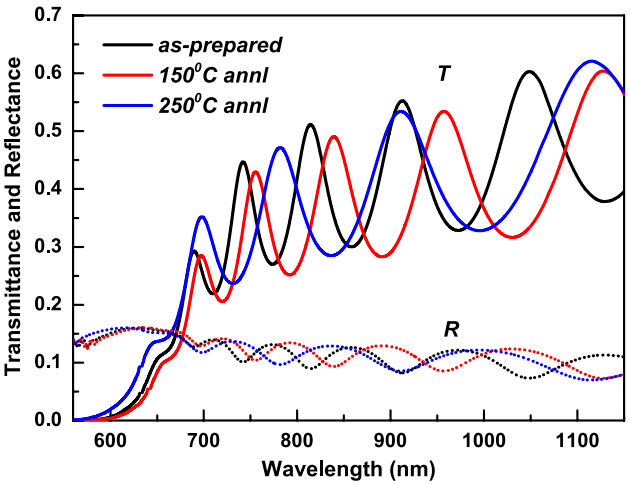

Fig. 5 *T* and *R* spectra of the films

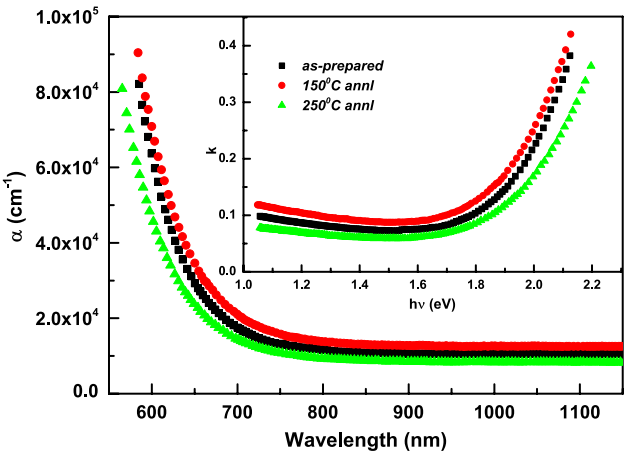

Fig. 6 α and k of the studied films

5.1.1.4 Optical density (OD) There is another parameter that describes the ability to absorb the electromagnetic radiation, known as optical density. This term characterizes the propagation of electromagnetic radiation through the material system that can be used to manufacture several

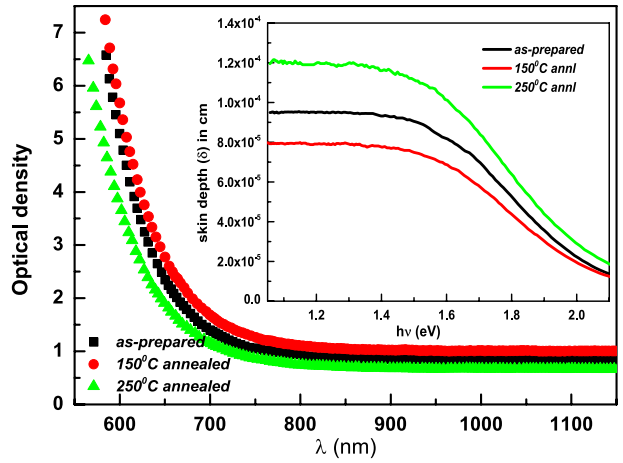

Fig. 7 Variation of OD with λ

optoelectronic devices. Furthermore, the optical density is related to 'α' by the relation [33]:

$$\text{Optical density (OD)} = \alpha\, x\, d, \tag{3}$$

where α and d represent the absorption coefficient and film thickness (~800 nm).

The behavior of optical density with wavelength for as-deposited and the film annealed at 150 °C and 250 °C is shown in Fig. 7 which shows the decrease of optical density with wavelength up about 680 nm and then saturated. This abrupt decrease is almost the wavelength of the absorption edges of the studied film. Then the optical density systematically decreased with the increase in 'λ' for all the films. In addition, it was observed the opposite changes in the OD values with annealing at 150 °C and 250 °C, respectively.

5.1.1.5 Skin depth (δ) The change in the skin depth or penetration depth (δ) of the studied thin films upon incident radiation energy can be estimated from the reciprocal of the absorption coefficient (α):

$$\text{Skin depth}(\delta) = 1/\alpha. \tag{4}$$

This behavior relates to the exponential behavior of the amplitude of the electromagnetic waves after overpassing the film thickness [33]. Then the skin depth of the film is defined by

$$\delta(\text{cm}) = d.\ln\left[\frac{T}{(1-R)^2}\right], \tag{5}$$

where d represents film thickness, T and R are the transmittance and reflectance data of the studied films. Figure 7 (inset) depicts that skin depth decreased for 150 °C annealed film, whereas increased with annealing temperature 250 °C. Furthermore, when the energy of the incident radiation increased the skin depth is dramatically decreased for all films near to zero value.

It is also noted that there is a directly proportional interrelation between skin depth (δ) and optical energy bandgap (E_g). This relation comes from the dependency over the optical conductivity as both are dependent on conductivity.

5.2 Optical bandgap (E_g) and Tauc parameter ($B^{1/2}$)

Using the values of 'α', the optical bandgap (E_g) of the system was evaluated from the Tauc formula (for $\alpha \geq 10^4$ cm^{-1}) [34]:

$$\alpha h\nu = B\left(h\nu - E_g^{\text{Opt}}\right)^m, \tag{6}$$

where B represents the Tauc parameter and m is a parameter related to the kind of electronic transition responsible for electron and absorption in both the valence and conduction band. According to Mott and Davis model [35] for amorphous semiconductor 'm' has several values depending on the type of transitions taking place inside the system like m=½, 3/2, 2, and 3 for direct allowed, direct forbidden, indirect allowed and indirect forbidden transition, respectively. Here, m=2 fits for the analysis of $As_{35}Se_{65}$ thin film samples which represent an indirect allowed transition process.

Figure 8 represents the variations of $(\alpha h\nu)^{1/2}$ vs incident energy ($h\nu$) of as-deposited and annealed thin films from which energy bandgap (E_g) is obtained from intercept of the linear portion of spectra with the X-axis ($(\alpha h\nu)^{1/2}$=0). The obtained E_g values are tabulated in Table 2 that shows the decrease of bandgap from 1.66 eV (as-prepared) to 1.62 eV for 150 °C annealed film and increased to 1.68 eV for the 250 °C annealed film which was annealed above T_g.

The reduction of the optical energy bandgap upon annealing below T_g may be explained through the Mott and Davis model [35]. As per the model, annealing causes the breakdown

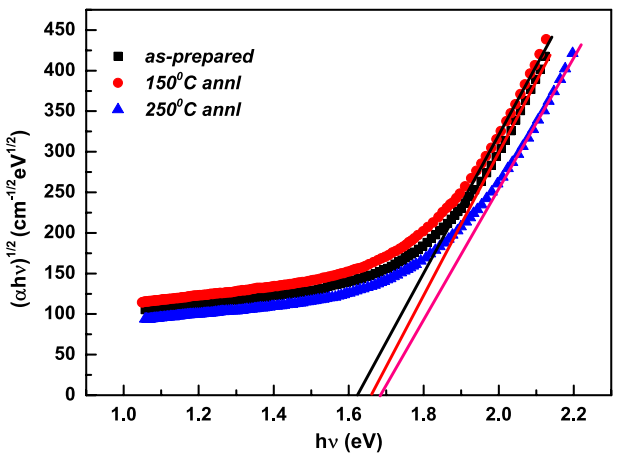

Fig. 8 $(\alpha h\nu)1/2$ vs $h\nu$ for the studied films

Table 2 Optical parameters of the studied films

Optical parameters	As-prepared	150 °C annealed	250 °C annealed
Bandgap (E_g) eV	1.66	1.62	1.68
Tauc parameter ($B^{1/2}$) $cm^{-1/2}$ $eV^{-1/2}$	898	869	911
Urbach energy (E_u) meV	188	217	172
Dispersion or strength energy, E_d (eV)	18.44	21.07	17.76
Single oscillator energy E_0 (eV)	2.51	2.57	2.50
The first moments of the optical spectra, M_{-1}	7.346	8.198	7.104
The second moments of optical spectra, M_{-3}	1.166	1.241	1.136
Static refractive index (n_0)	2.889	3.032	2.846
High-frequency dielectric constant ($\varepsilon_\infty = n_0^2$)	8.346	9.193	8.099
Oscillator strength $f = E_0E_d$	46.284	54.149	44.4
Dielectric constant of the lattice (ε_L)	17.233	17.704	16.853
Carrier concentration N/m^*	8.335×10^{39}	7.368×10^{39}	8.141×10^{39}
Oscillator wavelength, λ_0 (nm)	489.8	483.59	492.85
oscillator strength (s_0) nm^2	3.09×10^{-5}	3.50×10^{-5}	2.91×10^{-5}
First order nonlinear susceptibility (χ^1)	0.585	0.652	0.565
Third-order nonlinear susceptibility (χ^3)	1.99×10^{-11}	3.07×10^{-11}	1.73×10^{-11}
Nonlinear refractive index (n_2)	2.59×10^{-10}	3.81×10^{-10}	2.29×10^{-10}

of the weaker bonds to form surface dangling bonds which are responsible for the formation of localized states in the bandgap region. Such localized states form band-tail, that decreases the optical bandgap like other studies due to the annealing effect [36, 37]. However, the increase in E_g value for the 250 °C annealed film may be due to the reduction of defect states and an increase in structural ordering which is noticed from the $B^{1/2}$ values. Due to annealing, dangling bond defects along with some unsaturated bonds gradually annealed out by forming more saturated bonds. Thus, the decrease of unsaturated bonds causes decrease in the density of localized states which consequently increases the optical bandgap [38, 39].

The observed E_g value shows a good correlation with the skin depth spectra as skin depth is less for 150 °C annealed film which has reduced the bandgap and skin depth is more for the 250 °C annealed film which has increased bandgap. The measurement of the degree of disorder ($B^{1/2}$) has been done by calculating the slope from Fig. 8 fitting and shown in Table 2. It was observed that the value of Tauc parameter decreased for 150 °C annealed film and increased for 250 °C annealed film.

5.2.1 Urbach energy (E_u)

In the amorphous chalcogenide system, the absorption edges observed differently by showing an exponential behavior with incident energy ($h\nu$) near the absorption edges as represented by Urbach relation [40]:

$$\alpha(h\nu) = \alpha_0 e^{\frac{h\nu}{E_u}}, \tag{7}$$

where α_0 is a constant and E_u represents the Urbach Energy which was calculated from the slope of the straight line drawn in the plot $\ln(\alpha/\alpha_0)$ vs ($h\nu$). The values of E_u, which was estimated from the slope ($1/E_u$) of the spectra are listed in Table 2. The Urbach energy is being interpreted as the width of the tails of the localized states present in the gap region and measures the degree of disorder in amorphous semiconductor systems. It is seen that the Urbach energy increased for 150 °C annealed film and decreased for 250 °C annealed film. The increase/decrease of E_u and decrease/increase of E_g with annealing temperature can be attributed to the increase/decrease of the degree of disorder which results in an increase/decrease of the band tailing, and consequently a decrease/increase of E_g values [41, 42].

5.2.2 Linear refractive index (n)

Most of the calculation of the refractive index and thickness of the films by Swanepoel's envelope method [43] has been proved approximately correct. According to this method, the first approximation refractive index (n_1) for the region of weak and moderate absorption can be estimated according to the equation:

$$n_1^2 = \left[N + \left(N^2 - S^2\right)^{1/2}\right]. \tag{8}$$

where

$$N = 2S\left(\frac{T_M - T_m}{T_M T_m}\right) + \left(\frac{S^2+1}{2}\right), \tag{9}$$

where T_m and T_M are the minima and maxima of transmittance at fixed λ and 'S' represents substrate refractive index (1.51). By following the procedures as detailed in

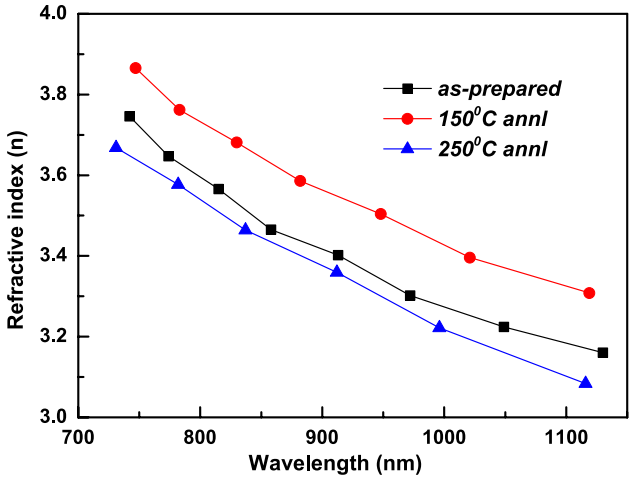

Fig. 9 n vs λ plot of the studied films

Ref. [43], the actual refractive index of the films at different wavelengths was estimated and is shown in Fig. 9. It was observed that the refractive index decreased with increases of the wavelength which is attributed towards the normal dispersion of the studied films. It also shows that the refractive index increased for 150 °C annealed film from the as-prepared film, whereas decreased with annealing at 250 °C. This behavior of the refractive index satisfies the Moss rule, i.e., $E_g n^4 \sim$ constant [44] and studied by other others in different materials [45, 46].

5.2.3 Single oscillator energy (E_0) and dispersion energy (E_d)

Wemple-Di Domenico (WDD) single effective oscillator model [47] is based on refractive index dispersion of the system which gives an inherent physical explanation of the measured parameters by just fitting the experimental data [33]. This model provides two main outputs; dispersion energy (E_d) and effective single oscillator energy (E_0). The E_0 is also known as an average of the energy gap that describes the information regarding the overall band structure of the system which is completely different from E_g, but there exists an empirical relation between E_0 and E_g, i.e., $E_0 \approx 2E_g$ [48]. However, in our case, the E_0 value is not exactly double of the E_g value. Similarly, the dispersion energy E_d signifies the oscillator strength that is related to the interband optical transition of the system.

According to the WDD dispersion theory, the 'n' value is related to $h\nu$, E_0 and E_d through the relation:

$$(n^2-1) = \frac{E_0 E_d}{E_0^2 - (h\vartheta)^2}, \tag{10}$$

which can also be written as;

$$(n^2-1)^{-1} = \frac{E_0^2 - (h\vartheta)^2}{E_0 E_d} = \frac{E_0}{E_d} - \frac{(h\vartheta)^2}{E_0 E_d}. \tag{11}$$

The dependency of $(n^2-1)^{-1}$ with $(h\nu)^2$ is graphically represented in Fig. 10. The slope of the straight lines in Fig. 10 represents $(1/E_0E_d)$ and the intercept with Y-axis represents (E_0/E_d). From the value of slope and intercept, the energy value of E_0 and E_d was evaluated and shown in Table 2. It is observed that for annealing at a temperature below T_g, i.e., at 150 °C, results in the increase of E_0 and E_d, whereas the opposite behavior was observed in the case of annealing at 250 °C. This behavior is quite similar to the behavior shown by the optical energy bandgap.

The first and second moments of the optical spectra, i.e., M_{-1} and M_{-3} were evaluated from the obtained E_0 and E_d values using the WDD model. These moments can be deduced as.

$$E_0^2 = \frac{M_{-1}}{M_{-3}}, \text{ and } E_d^2 = \frac{M_{-1}^3}{M_{-3}}. \tag{12}$$

The above equations can be written as,

$$M_{-1} = \frac{E_d}{E_0}, \text{ and } M_{-3} = \frac{M_{-1}}{E_d^2}. \tag{13}$$

Using the above relations, the first order and third-order moment of optical spectra were calculated and listed in Table 2. It was observed that the value of the moments, first increased for 150 °C annealing and then decreased for 250 °C annealing.

Similarly, from the single oscillator effective model, the value of dielectric constant (ε_∞), as well as static refractive index (n_0), can also be evaluated using the value of E_0 and E_d by the formula [49]:

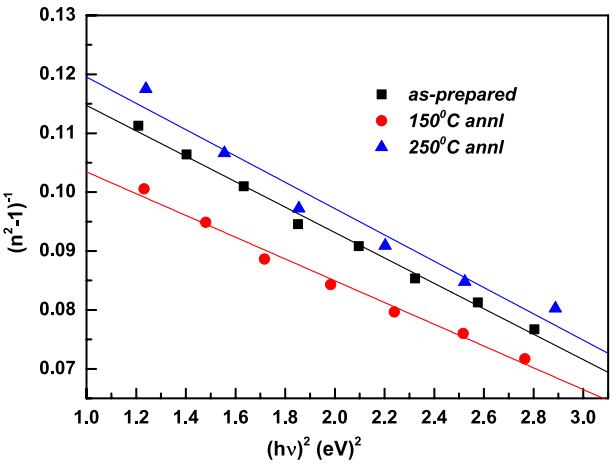

Fig. 10 $(n^2-1)^{-1}$ vs $(h\nu)^2$ of the films

$$\varepsilon_\infty = 1 + \frac{E_d}{E_0}, \text{ and } n_0 = \sqrt{1 + \frac{E_d}{E_0}}, \tag{14}$$

$\varepsilon_\infty = (n_0)^2$, denoted as the real dielectric constant of the lattice.

The calculated dielectric constant (ε_∞) and static refractive index (n_0) are presented in Table 2. Like the other parameters, the value of ε_∞ and n_0 first increased for annealing at 150 °C and then decreased further for annealing at 250 °C. The oscillator strength of the films is given by [50]

$$F = E_0 E_d. \tag{15}$$

The oscillator strength values are presented in Table 2 which shows the increase of strength with annealing at 150 °C and then decreased for annealing at 250 °C.

5.2.4 Carrier concentration (N/m^*) and high-frequency dielectric constant (ε_L)

Upon using the linear refractive index values, the dielectric constant (ε_L) and the ratio of carrier concentration per effective mass (N/m^*) was calculated by plotting n^2 with λ^2 (Fig. 11) through the following equation:

$$n^2 = \varepsilon_1 = \varepsilon_L - \left(\frac{e^2}{4\pi^2 c^2 \varepsilon_0}\right)\left(\frac{N}{m^*}\right)\lambda^2, \tag{16}$$

where ε_L represents the real part of dielectric constant, N is the free charge carrier concentration, ε_0 is the permittivity of free space, m^* is the effective mass of the free charge carriers and c is the velocity of light. The ε_L is related to free charge carrier concentration and its effect contributed to the polarization process inside the material [51]. Here, the slope and intercepts with the X-axis are represented as N/m^* and ε_L. The obtained value of N/m^* and ε_L are listed in Table 2. The value of N/m^* first decreased for annealing below T_g, i.e., at 150 °C and then increased for annealing at 250 °C. However, the ε_L value increased for 150 °C annealed film and decreased for annealing at 250 °C film.

5.2.5 Oscillator wavelength (λ_0) and strength of oscillator (S_0)

As per the single oscillator model proposed by Sellmeier, the refractive index at low frequency applied for classical dispersion relation is given as [52]

$$\frac{n_0^2 - 1}{n^2 - 1} = 1 - \frac{\lambda_0^2}{\lambda^2}. \tag{17}$$

$$\frac{1}{n^2 - 1} = \frac{1}{n_0^2 - 1} - \frac{\lambda_0^2}{\left(n_0^2 - 1\right)\lambda^2}. \tag{18}$$

After rewriting Eq. (18) becomes:

$$(n^2 - 1)^{-1} = \frac{1}{s_0 \lambda_0^2} - \frac{1}{s_0 \lambda^2}, \tag{19}$$

where $(n_0^2 - 1)$ has been replaced with s_0. A graph between $(n^2 - 1)^{-1}$ vs $(\lambda)^{-2}$ was plotted from Eq. (19), as shown in Fig. 12. From the straight-line fitting, we have obtained $\frac{1}{s_0 \lambda_0^2}$ as its Y-intercept and $\frac{1}{s_0}$ as its slope. From the values of Y-intercept and the slope, the values of oscillator wavelength (λ_0) and oscillator strength (s_0) were obtained and shown in Table 2. It was observed that the value of λ_0 and S_0 are showing the opposite behavior with each other.

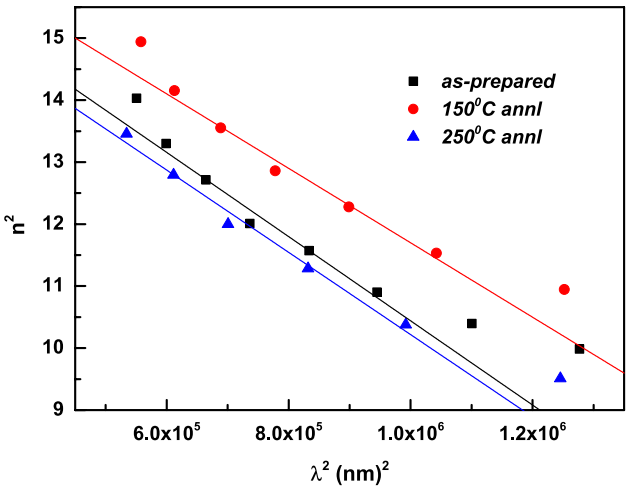

Fig. 11 n^2 vs λ^2 plot of the studied films

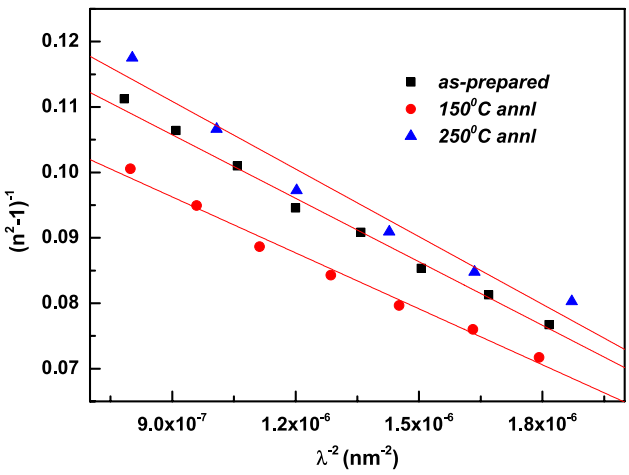

Fig. 12 $(n^2 - 1)^{-1}$ vs $1/\lambda^2$ plot of the studied films

5.2.6 Non-linear optical properties

5.2.6.1 Third-order non-linear susceptibility ($\chi^{(3)}$) The nonlinear effects come into action when there are sufficiently high and intense incident energy falls on the film that can alter the properties of the system. This nonlinearity expresses itself through the polarization of the material system. Furthermore, the amorphous chalcogenide system possesses higher value of the optical non-linear susceptibility which helps to manufacture several non-linear optical devices [53]. Ticha and Tichy [54] and Miller's rule [55] combination with Wemple–DiDomenico model was used to estimate the $\chi^{(3)}$, since E_d and E_0 are related to the chemistry of the material. The expression for Miller's principle is

$$\chi^{(3)} = \frac{A\left(n_0^2 - 1\right)^4}{(4\pi)^4}. \tag{20}$$

It can be also expressed in the form of:

$$\chi^{(3)} = A\left[\chi^{(1)}\right]^4 \text{ where } \chi^{(1)} = \frac{\left(n_0^2 - 1\right)}{4\pi}. \tag{21}$$

In the above-mentioned expressions, n_0 is the static refractive index in the $\lim_{h\nu\sim 0}\left(n = n_0\right)$ and A is a constant equal to 1.7×10^{-10} esu. Equations (20) and (21) are the combined relation of Miller's principle and WDD model suggested by Tichy et al. [54].

Table 2 presents the estimated $\chi^{(1)}$, $\chi^{(3)}$ values from which it was found that the susceptibility increased for annealing below T_g, i.e., at 150 °C, and decreased for annealing at 250 °C. This increase/decrease in susceptibility due to annealing can be explained by homogenization and polymerization [56]. The presence of lone pair orbitals in chalcogenides makes them polarized easily and plays an important role in nonlinear effects also.

5.2.7 Non-linear refractive index (n_2)

According to Miller's relation, the non-linear refractive index (n_2) can be written in terms of $\chi^{(3)}$ which has the form:

$$n_2 = \frac{12\pi\chi^3}{n_0}. \tag{22}$$

The obtained results indicate that the n_2 value increased for 150 °C annealed film and decreased for 250 °C annealed film. It shows the same behavior as that of the linear refractive index (n). This increase in nonlinearity upon annealing below T_g (at 150 °C) indicates an increase in different defect density states which can be explained through an increase in polarization of the system. The higher values of non-linear parameters make these annealing induced thin films diffraction free and suitable for non-linear devices. Due to the increase in structural order, the number of various defects in gap states decreased which leads to the reduction of nonlinearity for 250 °C annealed film. The reduction of n_2 and $\chi^{(3)}$ upon annealing at 250 °C can be useful for UV nonlinear materials and solid-state laser.

5.3 X-ray photoelectron spectroscopy (XPS) analysis

XPS is a surface analytic technique from which the information about different bonding can be obtained from the core-level analysis. The alterations in chemical bonding are often realized through correlation with chemical shifts in the XPS binding energies of key elements from their core-level spectra. Though the survey spectra consist of various core level and Auger spectra, we have selected the As 3*d* and Se 3*d* core-level peaks for the analysis. The core-level spectra were deconvoluted into sub peaks using the XPS data analysis software called XPSPEAK1. The Shirley baseline was used for background removal and the deconvoluted peaks were assumed to have Voigt line shapes. The deconvolution spectra give the spin–orbit splitting characteristic of the As3*d* and Se3*d* core levels. The spectrum was deconvolved into two doublets, each of them related to a specific state. During deconvolution of the peak, two constraints were considered for the process (i) the peak-to-peak separation and (ii) the 3*d* orbital peak area [57].

Due to spin orbit splitting, the Se3*d* peak consists Se3$d_{5/2}$ and Se3$d_{3/2}$ doublets with a peak-to-peak separation of ΔSe ≈ 0.79 eV, a value close to that found by Zhu et al. [58]. The Se3$d_{3/2}$ orbital which is generally at higher energy value corresponds to the Se atom bonded to two As atoms (As−Se−As), whereas the Se3$d_{5/2}$ orbital refers to the Se atoms with Se−Se−As bond found to be at lower BE [59]. Thus Se3$d_{5/2}$ orbital refers to the Se–Se homopolar bonds and Se3$d_{3/2}$ orbital refers to the As–Se heteropolar bonds. The deconvoluted Se3*d* core-level peak of the as-prepared, 150 °C annealed and 250 °C annealed film is shown in Fig. 13. The Se3$d_{5/2}$ and Se3$d_{3/2}$ peaks for the as-prepared film were at 54.15 eV and 54.94 eV, respectively. After 150 °C annealing, the Se3$d_{5/2}$ and Se3$d_{3/2}$ peaks were found at 54.99 eV and 54.20 eV with the area 1783 and 2014 units, respectively. The intensity of the 3$d_{5/2}$ peak is more than that of the 3$d_{3/2}$ peak for the 150 °C annealed film. This clearly shows the increase in Se–Se homopolar bond density than the As–Se heteropolar bond density which brought more disorder in the film. But it was observed that the intensity of 3$d_{5/2}$ peak is less than that of the 3$d_{3/2}$ peak for the 250 °C annealed film with peak positions at 54.68 eV and 55.47 eV, respectively. The area of 3$d_{5/2}$ and Se3$d_{3/2}$ peaks is 338 and 464 units, respectively, which clearly shows the more heteropolar bond than the homopolar bond in 250 °C annealed film. The opposite nature of the peaks for the two annealed films is in accordance with the optical parameters

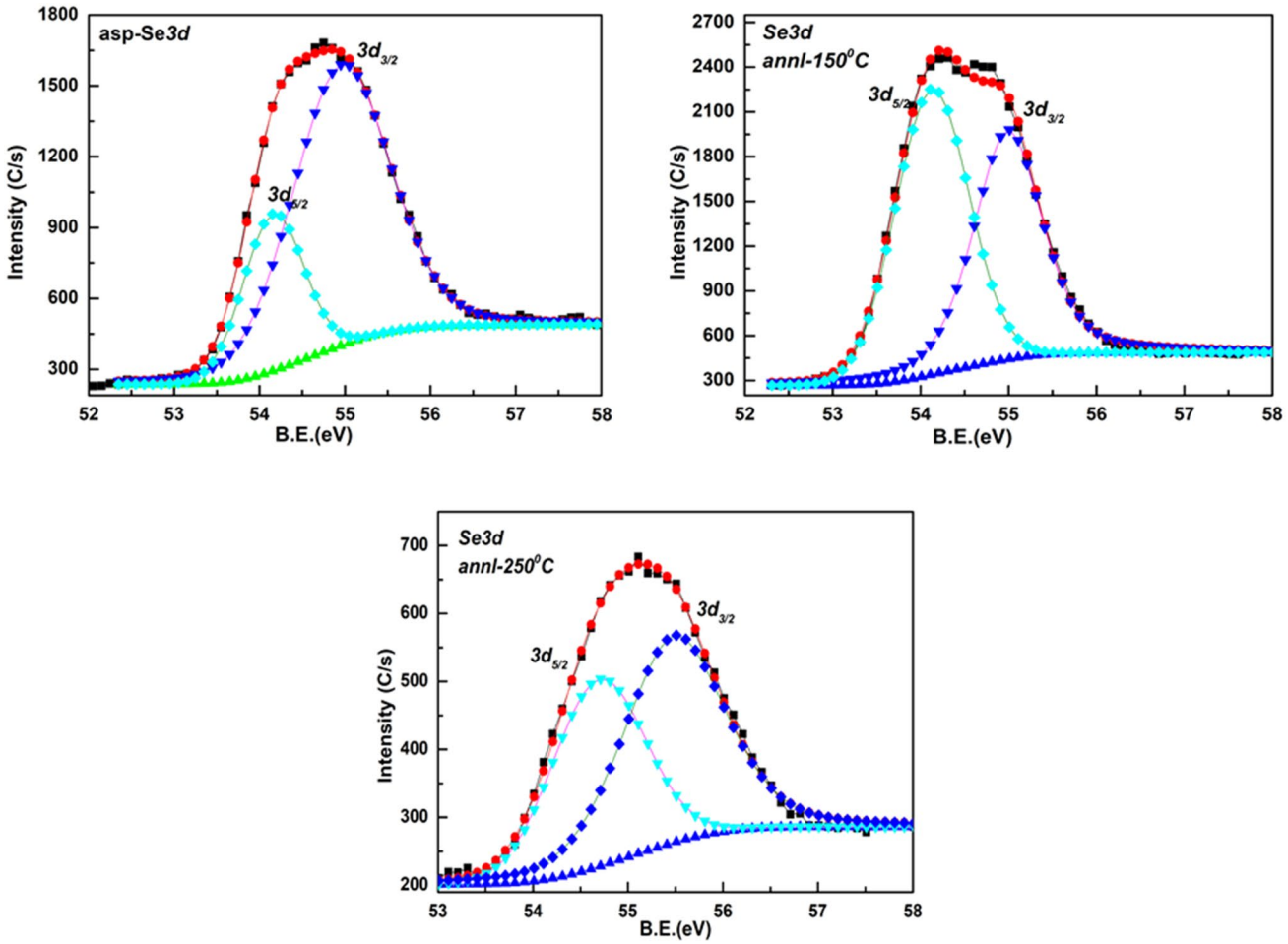

Fig. 13 Deconvoluted Se 3*d* core-level peak of the films

as observed. The full width half maximum (FWHM) for the Se3$d_{5/2}$ is more (0.99) than that of the Se3$d_{3/2}$ (0.91) for the 150 °C annealed film, whereas the FWHM for Se3$d_{5/2}$ is less (1.15) than that of the Se3$d_{3/2}$ (1.26) for the 250 °C annealed film. The comparative value of peak intensity, FWHM and area under the peak for the two annealed films are opposite to each other.

The As3*d* spectra consists of two peaks corresponding to 5/2 and 3/2 spin states of the 3*d* orbital with a separation of $\Delta As \approx 0.70$ eV, a value close to that found by Beiyuan et al. [60]. For As 3d, the different bonding states are Se−As−Se_2 and As−As−Se_2. The sub peak $d_{3/2}$ in the deconvoluted As 3*d* is assigned as As atoms within $AsSe_{3/2}$ pyramidal units (Se−As−Se_2) at higher BE and the sub peaks $d_{5/2}$ is assigned as As atoms within units containing As–As homopolar bonds at lower BE, as shown in Fig. 14. Because As (2.18) has a smaller electro negativity than Se (2.55), the homopolar As–As bond containing units contribute the lower BE peak [61]. The peak intensity of As3$d_{5/2}$ (homopolar bond) is more than that of the As3$d_{3/2}$ (heteropolar) in the 150 °C annealed film which was opposite for the 250 °C annealed film. After 150 °C annealing, the As 3$d_{5/2}$ and As 3$d_{3/2}$ peaks were found at 42.11 eV and 42.82 eV with the area 1653 and 1077 units, respectively. This clearly shows the increase in As–As homopolar bond density than the As–Se heteropolar bond density which brought more disorder in the film. But it was observed that the intensity of 3$d_{5/2}$ peak is less than that of the 3$d_{3/2}$ peak for the 250 °C annealed film with peak positions at 42.60 eV and 43.19 eV, respectively. The area of As3$d_{5/2}$ and As3$d_{3/2}$ peaks is 101 and 602 units, respectively, which clearly shows the more heteropolar bond than the homopolar bond in 250 °C annealed film. The full width half maximum (FWHM) for the As3$d_{5/2}$ is more (0.78) than that of the As3$d_{3/2}$ (0.69) for the 150 °C annealed film, whereas the FWHM for As3$d_{5/2}$ is less (0.53) than that of the As3$d_{3/2}$ (1.12) for the 250 °C annealed film. The opposite nature of the peaks for the two annealed films is in accordance with the optical parameters as observed.

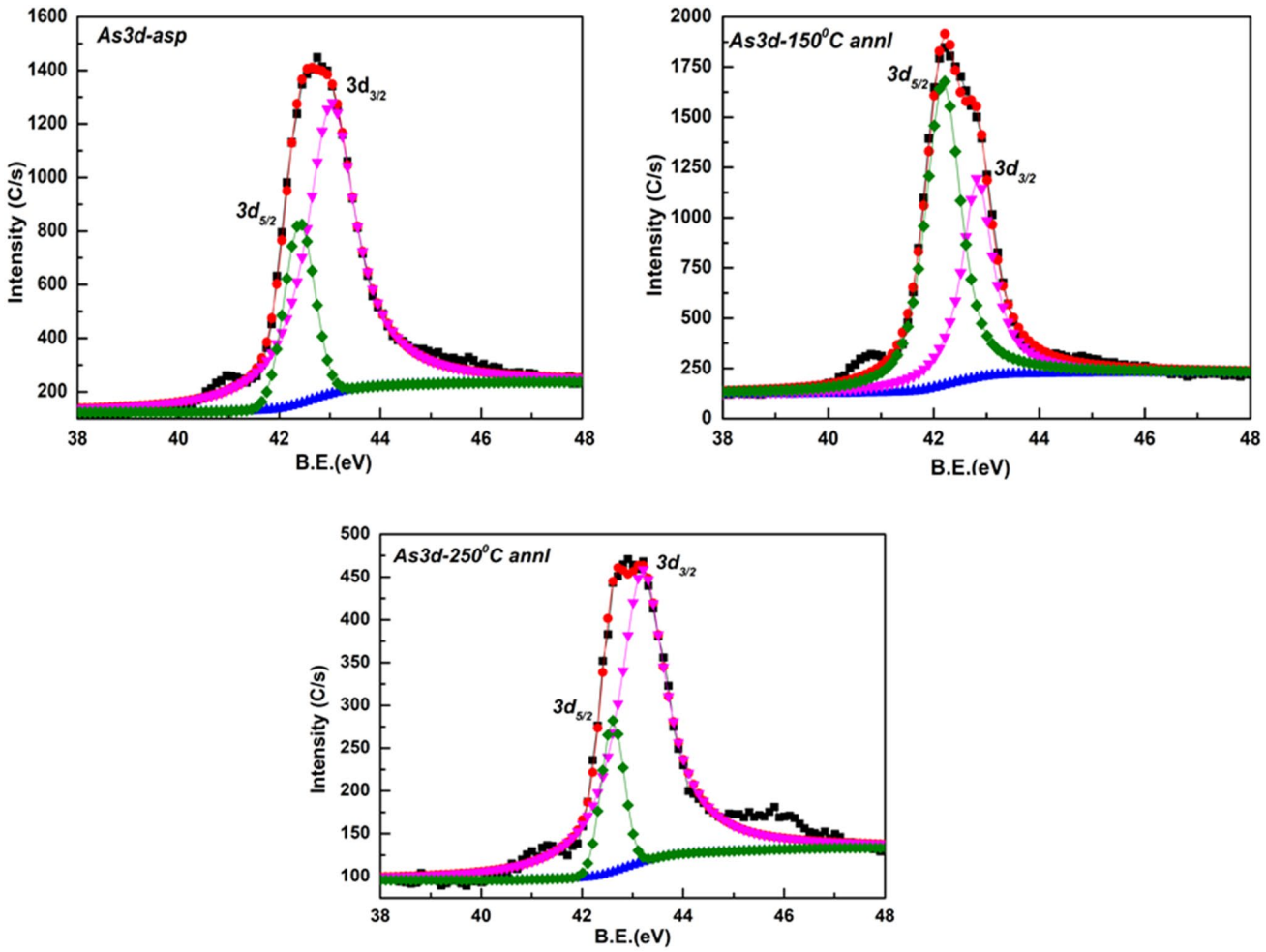

Fig. 14 Deconvoluted As 3*d* core-level peak of the films

6 Conclusions

The optical measurements of as-prepared and annealed $As_{35}Se_{65}$ films was calculated and studied by several models. Both the linear and nonlinear optical parameters have shown the opposite change for 150 °C and 250 °C annealed films. The optical band gap decreased for 150 °C annealed film, whereas it increased for the 250 °C annealed film. The linear refractive index, nonlinear refractive index, third-order susceptibility increased/decreased for the 150 °C and 250 °C annealed films, whereas carrier concentration and oscillator wavelength showed opposite changes. The annealing at both the temperature, however, did not show any change in the amorphous structure, but the degree of disorder in the film altered which was noticed from the Tauc parameter, Urbach energy, and Raman spectra. The skin depth increased and optical density decreased for the 150 °C annealed film which showed opposite changes for the 250 °C annealed film. The dispersion energy and oscillator energy increased for the 150 °C annealed film which decreased for the 250 °C annealed film. The deconvoluted XPS core-level peak intensity and area change showed the homopolar and heteropolar bond concentration that affected the degree of disorder. Therefore, we have observed both decrease/increase in the optical parameters when annealed at 150 °C and 250 °C temperatures. Such types of dual changes in the film at two different temperatures can be used for the fabrication of various optical devices based on their requirement.

Acknowledgements The author Dr. Naik would like to thank ICT-IOC, Bhubaneswar for the Start-up Research grant, and the Department of Physics, Indian Institute of Science (IISc.) for Optical, XPS, and Raman measurements. The usage of MNCF and NNCF facilities supported by Meity, DST and MOE are acknowledged.

Compliance with ethical standards

Conflict of interest There are no conflicts of interest for this manuscript.

References

1. G.K. Ahluwalia (ed.), *Applications of Chalcogenides: S, Se, and Te* (Springer, Berlin, 2017)
2. R. Manivannan, S.N. Victoria, Preparation of chalcogenide thin films using electrodeposition method for solar cell applications—a review. Sol. Energy **173**, 1144–1157 (2018)
3. T.V. Moreno, L.C. Malacarne, M.L. Baesso, W. Qu, E. Dy, Z. Xieb, J. Fahlman, J. Shen, N.G.C. Astrath, Potentiometric sensors with chalcogenide glasses as sensitive membranes: a short review. J. Non-Cryst. Solids **495**, 8–18 (2018)
4. S. Mishra, P.K. Singh, P. Lohia, D.K. Dwivedi, Arsenic modified $(Ge_{11.5}Te_{12.5}Se_{67.5})_{100-x}$ compound for IR application. J. Non-Cryst. Solids **547**, 120309 (2020)
5. J.L. Adam, X. Zhang, *Chalcogenide Glasses: Preparation, Properties and Applications* (Woodhead Publishing Limited, Cambridge, 2013)
6. M. Behera, C. Sripan, R. Ganesan, N.C. Mishra, R. Naik, Influence of Bi content on linear and nonlinear optical properties of $As_{40}Se_{60-x}Bi_x$ chalcogenide thin films. Curr. Appl. Phys. **19**(8), 884–893 (2019)
7. R. Naik, A. Jain, R. Ganesan, K.S. Sangunni, Compositional dependence optical properties study of $As_{40}Se_{60-x}Sb_x$ thin films. Thin Solid Films **520**, 2510–2513 (2012)
8. D. Sahoo, P. Priyadarshini, A. Aparimita, D. Alagarasan, S. Varadharajaperumal, R. Ganesan, R. Naik, Role of annealing temperature on optimizing the linear and nonlinear optical properties of $As_{40}Se_{50}Ge_{10}$ films. RSC Adv. **10**, 26675–26685 (2020)
9. A. Aparimita, P. Khan, J.R. Aswin, K.V. Adarsh, R. Naik, Role of thermal and photo annealing on nonlinear optical response of $Ge_{30}Se_{55}Bi_{15}$ thin films. J. Appl. Phys. **127**(7), 075102 (2020)
10. A.A. Shaheen, M.M.A. Imran, O.A. Lafi, M.I. Awadallah, M.K. Abdullah, Optical properties of a-$Se_{90}In_{10-x}Sn_x$ chalcogenide thin films before and after gamma irradiation. Rad. Phys. Chem. **79**(9), 923–928 (2010)
11. A.A.A. Darwish, H.A.M. Ali, On annealing induced effect in optical properties of amorphous GeSeSn chalcogenide films for optoelectronic applications. J. Alloys Compd. **710**, 431–435 (2017)
12. R.P. Wang, S.J. Madden, C.J. Zha, A.V. Rode, Annealing induced phase transformations in amorphous As_2S_3 films. J. Appl. Phys. **100**, 063524 (2006)
13. L. Tichy, H. Ticha, Covalent bond approach to the glass transition temperature of chalcogenide glasses. J. Non-Cryst. Solids **189**, 141–146 (1995)
14. B. Gleason, P. Wachtel, J.D. Musgraves, A. Qiao, N. Anheier, K. Richardson, Compositional tailoring of optical properties in IR transparent chalcogenide glasses for precision glass molding. Proc. SPIE **8884**, 888417–888427 (2013)
15. A. Siokou, M. Kalyva, S.N. Yannopoulos, M. Frumar, P. Nemec, Photoemission studies of As_xSe_{100-x} (x–0, 50, 100) films prepared by pulsed-laser deposition—the effect of annealing. J. Phys. Condens. Mat. **18**, 5525–5534 (2006)
16. T. Tsvetkova, S. Balabanov, E. Skordeva, S. Kitova, J. Sielanko, D. Maczka, J. Zuk, Surface morphology effects of post-implantation annealing in thin amorphous films of the As–Se system. Vacuum **72**, 143–147 (2004)
17. Y. Zou, H. Lin, O. Ogbuu, L. Li, S. Danto, S. Novak, J. Novak, J.D. Musgraves, K. Richardson, J. Hu, Effect of annealing condition on the physio-chemical properties of spin-coated As_2Se_3 chalcogenide glass films. Opt. Mater. Exp. **2**, 1723–1732 (2012)
18. M. Kalyva, A. Siokou, S.N. Yannopoulos, P. Nemec, M. Frumar, Electronic and structural changes induced by irradiation or annealing in pulsed laser deposited $As_{50}Se_{50}$ films—an XPS and UPS study. J. Phys. Chem. Solids **68**, 906–910 (2007)
19. P. Pradhan, P. Khan, J.R. Aswin, K.V. Adarsh, R. Naik, N. Das, A.K. Panda, Quantification of non-linear absorption in ternary As–Sb–Se chalcogenide glasses. J. Appl. Phys. **125**, 015105 (2019)
20. N. Charlie, N.C. Anheier, H.A. Qiao, B. Bernacki, M.C. Phillips, L. Petit, J.D. Musgraves, K. Richardson, Measurement of the refractive index dispersion of As_2Se_3 bulk glass and thin films prior to and after laser irradiation and annealing using prism coupling in the near and mid-infrared spectral range. Rev. Sci. Instrum. **82**, 053103 (2011)
21. P. Guo, C. Dong Li, W. Hung, W. Zhang, P. Zhang, T. Xu, Thermal annealing of Ge–Se thin films and its influence on waveguide performance. Opt. Mater. Exp. **10**, 129–137 (2020)
22. Y. Zhang, Y. Xu, P. Zhang, C. You, S. Zhang, M. Xie, N. Long, J. Tang, S. Dai, Femtosecond-laser-induced submicron grating periodic structures on As_2S_3 and $As_{35}Se_{65}$ glasses. Opt. Laser Tech. **108**, 306–309 (2018)
23. T.L. Barr, S. Seal, Nature of the use of adventitious carbon as a binding energy standard. J. Vac. Sci. Technol. A **13**, 1239 (1995)
24. R. Naik, K.V. Adarsh, R. Ganesan, K.S. Sangunni, S. Kokenyesi, U. Deshpande, T. Shripathi, X-ray photoelectron spectroscopic studies on Se/As_2S_3 and Sb/As_2S_3 nanomultilayered film. J. Non-Cryst. Solids **355**, 37–42 (2009)
25. J.P. De Neufville, S.C. Moss, S.R. Ovshinsky, Photo-structural transformations in amorphous As_2Se_3 and As_2S_3 films. J. Non-Cryst. Solids **13**, 191–223 (1974)
26. P. Pradhan, R. Naik, N. Das, A.K. Panda, Band gap tuning in $As_{40}Se_{53}Sb_{07}$ thin films by 532 nm laser irradiation: an optical investigation by spectroscopic techniques. Opt. Mater. **75**, 699–709 (2018)
27. P. Nemec, T.J. Jedelsky, M. Frumar, Z. Cernosek, Structure, optical properties and their photo-induced changes in As_xSe_{100-x} (x = 50, 57.1, 60) amorphous thin films prepared by pulsed laser deposition. Thin Solid Films **484**, 140–145 (2005)
28. M. Kudryashov, L. Mochalova, A. Nezdanov, R. Kornev, A. Logunov, D. Usanov, A. Mashina, G.D. Filpod, D. Gogova, A novel plasma-based method for synthesis of As–Se–Te films: impact of plasma parameters on the structure, composition, and optical properties. Super. Microstr. **128**, 334–341 (2019)
29. R. Naik, C. Sripan, R. Ganesan, Photo darkening in $As_{50}Se_{50}$ thin film by 532 nm laser irradiation. Opt. Laser Technol. **90**, 158–164 (2017)
30. M. Ahmad, P. Kumar, R. Thangaraj, Effect of isoelectronic substitution of Bi on the photoelectrical properties in amorphous Sn–Sb–Se films. Thin Solid Films **517**, 5965–5968 (2009)
31. S.A. Khan, J.K. Lal, A.A. Al-Ghamdi, Thermal annealing effect on optical constants of vacuum evaporated $Se_{75}S_{25-x}Cd_x$ chalcogenide thin films. Opt. Laser. Technol. **42**, 839–844 (2010)
32. S.A. Gad, H. Shaban, B.A. Mansour, G.M. Mahmoud, Determination and analysis of linear and nonlinear optical properties and electrical conductivity of amorphous $Pb_xGe_{42-x}Se_{48}Te_{10}$ thin films. Appl. Phys. A **126**, 354 (2020)
33. A.S. Hassanien, A.A. Akl, Influence of composition on optical and dispersion parameters of thermally evaporated non-crystalline $Cd_{50}S_{50-x}Se_x$ thin films. J. Alloy. Compd. **648**, 280–290 (2015)
34. J. Tauc, *Amorphous and Liquid Semiconductors* (Plenum Press, New York, 1974), p. 171
35. N.F. Mott, E.A. Davis, *Electronics Processes in Non-Crystalline Materials* (Clarendon, Oxford, 1979), p. 428
36. H.E. Atyia, N.A. Hageb, Influence of thermal treatment on the optical aspects for $Ge_{20}In_5Se_{75}$ films. Optik **127**, 3888–3894 (2016)
37. A. Aparimita, R. Naik, C. Sripan, R. Ganesan, Annealing induced transformations in structural and optical properties of $Ge_{30}Se_{70-x}Bi_x$ thin films. Phase Trans. **92**(8), 683–698 (2019)

38. A.S. Soltan, M. Abu El-Oyoun, A.A. Abu-Sehly, A.Y. Abdel-Latief, Thermal annealing dependence of the structural, optical and electrical properties of selenium–tellurium films. Mat. Chem. Phys. **82**, 101–106 (2003)
39. M. Behera, S. Behera, R. Naik, Optical band gap tuning by laser induced Bi diffusion into As_2Se_3 film probed by spectroscopic techniques. RSC Adv. **7**, 18428–18437 (2017)
40. F. Urbach, The long-wavelength edge of photographic sensitivity and of the electronic absorption of solids. Phys. Rev. **92**, 1324 (1953)
41. S. Moustafa, M. Mohamed, M.A. Abdel-Rahim, Composition dependence of structural and optical properties of Ge_xSe_{100-x} semiconducting thin flms. Opt. Quant. Electron. **51**, 337 (2019)
42. R. Panda, R. Naik, N.C. Mishra, Thermal annealing induced evolution of $AgIn_5Se_8$ phase from Ag/In_2Se_3 bilayer thin film. J. Alloys Compd. **778**, 819–826 (2019)
43. R. Swanepoel, Determination of the thickness and optical constants of amorphous silicon. J. Phys. E Sci. Instrum. **16**, 1214–1222 (1983)
44. T.S. Moss, A relationship between the refractive index and the infra-red threshold of sensitivity for photoconductors. Proc. Phys. Soc. B **63**, 167 (1950)
45. K.A. Aly, H.H. Amer, A. Dahshan, Optical constants of thermally evaporated Se–Sb–Te films using only their transmission spectra. Mater. Chem. Phys. **113**, 690–695 (2009)
46. M. Behera, P. Naik, R. Panda, R. Naik, Role of Te on the spectroscopic properties of $As_{50}Se_{40}Te_{10}$ thin films: an extensive study by FTIR and Raman spectroscopy. Opt. Mater. **66**, 616–622 (2017)
47. S.H. Wemple, M. DiDomenico, Behavior of the electronic dielectric constant in covalent and ionic materials. Phys. Rev. B **3**, 1338 (1971)
48. M. Ashraf, S.M.J. Akhtar, A.F. Khan, Z. Ali, A. Qayyum, Effect of annealing on structural and optoelectronic properties of nanostructured Zn–Se thin films. J. Alloys Compd. **509**, 2414–2419 (2011)
49. D. Sahoo, P. Priyadarshini, A. Aparimita, D. Alagarasan, S. Varadharajaperumal, R. Ganesan, R. Naik, Optimization of linear and nonlinear optical parameters in $As_{40}Se_{60}$ film by annealing at different temperature. Optik **219**, 165286–165312 (2020)
50. M.M. El-Nahass, M.M. Sallam, M.A. Afifi, I.T. Zedan, Structural and optical properties of polycrystalline $CdSe_xTe_{1-x}$ ($0 \le x \le 0.4$) thin films. Mater. Res. Bull. **42**, 371–384 (2007)
51. M.M. El-Nahass, M.H. Ali, I.T. Zedan, Photoinduced changes in linear and non-linear optical properties of $Ge_{10}In_{10}Se_{80}$ thin films. J. Non-Cryst. Solids **404**, 78–83 (2014)
52. K.A. Aly, F.M. Abdel-Rahim, Effect of Sn addition on the optical constants of Ge–Sb–S thin films based only on their measured reflectance spectra. J. Alloy. Compd. **561**, 284–290 (2013)
53. I. Sharma, S.K. Tripathi, P.B. Barman, Thickness-dependent optical properties and non-linear refractive index of a Ge-Se-In thin films. Phase Trans. **87**, 363–375 (2014)
54. H. Ticha, L. Tichy, Semiempirical relation between non-linear susceptibility (refractive index) linear refractive index and optical gap and its application to amorphous chalcogenides. J. Optoelectr. Adv. Mater. **4**, 381–386 (2002)
55. J.J. Wayne, Optical third-order mixing in Ga–As, Ge, Si, and In–As. Phys. Rev. B **178**, 1295–1303 (1969)
56. N.M. Ravindra, V.K. Srivastava, Electronic polarizability as a function of the penn gap in semiconductors. Infrared Phys. **20**, 67–69 (1980)
57. M. Morales Luna, M.A. Arvizu, M.P. Gonzalez, S.A. Tomas, Effect of a CdSe layer on the thermo- and photochromic properties of MoO_3 thin films deposited by physical vapor deposition. J. Phys. Chem. C **123**, 17083–17091 (2019)
58. D. Zhu, A. Tang, Q. Kong, B. Zeng, C. Yang, F. Teng, Roles of sulfur sources in the formation of alloyed $Cu_{2-x}SySe_{1-y}$ nanocrystals: controllable synthesis and tuning of plasmonic resonance absorption. J. Phys. Chem. C **121**, 15922–15930 (2017)
59. A. Siokou, M. Kalvya, S.N. Yannopoulos, M. Frumar, P. Nemes, Nano-scale annealing-induced structural changes in As-rich pulsed laser deposited As_xSe_{100-x} films studied by XPS. J. Non-Cryst. Solids **352**, 1520 (2006)
60. J. Beiyuan, J. Shan-Li, D.C.W. Tsang, L. Wang, C.S. Poon, X.D. Li, S. Fendorf, Fate of arsenic before and after chemical-enhanced washing of an arsenic-containing soil in Hong Kong. Sci. Total Environ. **599–600**, 679–688 (2017)
61. W. Li, S. Seal, C. Rivero, C. Lopez, K. Richardson, A. Pope, A. Schulte, S. Myneni, H. Jain, K. Antoine, A.C. Miller, Role of ratio in chemical bonding of As–S–Se glasses investigated by Raman, X-ray photoelectron, and extended X-ray absorption fine structure spectroscopies. J. Appl. Phys. **98**, 053503 (2015)